Numerical Simulations of an Observed Gravity Current and Gravity Waves in an Environment Characterized by Complex Stratification and Shear

YI JIN, STEVEN E. KOCH, AND YUH-LANG LIN

Department of Marine, Earth, and Atmospheric Sciences, North Carolina State University, Raleigh, North Carolina

F. MARTIN RALPH

NOAA/ERL/Environmental Technology Laboratory, Boulder, Colorado

CHAING CHEN

Science Systems and Applications, Inc., Lanham, Maryland

ABSTRACT

Numerical simulations of a gravity current in an environment characterized by complex stratification and vertical wind shear have been performed using a nonhydrostatic, two-dimensional, dry, primitive-equation model. Data from one of the most complete documentations to date of gravity waves associated with a gravity current, presented in an earlier study, are used both to prescribe the gravity current's environment and for validation of the simulated gravity current and its associated gravity waves. These comparisons indicate that the gravity current observed by a Doppler wind profiler and sodars was well simulated in terms of depth, density contrast, and propagation speed and that the model produced a variety of gravity waves similar in many ways to those observed.

Because uncertainties remained concerning the gravity wave generation mechanisms derived from the observations (e.g., wavelengths were not observed), the validated simulations are used to test these tentative hypotheses. The simulations confirm that trapped lee-type gravity waves formed in response to flow over the head of the gravity current and that Kelvin–Helmholtz (KH) waves were created because of shear atop the cold air within the gravity current. The 2.8-km wavelength of the simulated KH waves agrees with the 2- to 3-km wavelength inferred from the observations. However, the 6.4-km wavelength of the simulated lee-type waves is significantly shorter than the 12.5-km wavelength inferred from the observational data, even though wave periods (20–23 minutes) are nearly identical. Sensitivity tests indicate that the curvature in the wind profile associated with the low-level opposing inflow and an elevated isothermal layer worked together to support the development of the trapped lee-type waves. The model produces a deep vertically propagating wave above the gravity current head that was not present in the observations. As deduced in the earlier study, sensitivity tests indicate that the prefrontal, near-surface stable layer was too shallow to support the generation of a bore; that is, conditions were supercritical. Synthesis of detailed observations and numerical simulations of these mesoscale phenomena thus offers the broadest examination possible of the complex physical processes.

1. Introduction

Gravity waves are ubiquitous mesoscale features of the atmosphere that can cause large vertical motions and can propagate great distances. They may, for example, trigger instabilities that lead to the development of severe weather or act as a dissipation mechanism. Two ways by which gravity waves are generated are shear instability and external forcing. Gravity currents often create conditions conducive to shear instability,

but can also serve as an external forcing mechanism capable of producing gravity waves under certain environmental conditions. Observational studies (Charba 1974; Marks 1974; Goff 1976; Carbone 1982; Wakimoto 1982; Wang et al. 1983; Doviak and Ge 1984; Mueller and Carbone 1987; Fulton et al. 1990; Koch et al. 1991; Mahapatra et al. 1991; Parsons et al. 1991; Ralph et al. 1993), laboratory models (Rottman and Simpson 1989), and numerical simulations (Droegemeier and Wilhelmson 1985a,b; Haase and Smith 1989a,b; Raymond and Rotunno 1989; Lin and Chun 1991) have been used to study gravity currents and their associated gravity wave activity. Various kinds of gravity waves associated with a gravity current may occur depending on atmospheric stratification and wind shear. An undular bore is an example of one such wave

Corresponding author address: Dr. Steven E. Koch, Department of Marine, Earth, and Atmospheric Sciences, North Carolina State University, Box 8208, Raleigh, NC 27695-8208.
E-mail: Steve_Koch@ncsu.edu

disturbance. The bore causes a sudden increase in depth of a shallow stable layer. Another closely related phenomenon evolving from the gravity current is the solitary wave—a single symmetric gravity wave that can propagate hundreds of miles from the source region without much change in its form because of a balance between frequency dispersion and nonlinear wave steepening effects (Mahapatra et al. 1991). Another interesting phenomenon is Kelvin–Helmholtz (KH) wave activity resulting from the instability associated with significant wind shear and density contrast usually existing at the top of the gravity current (Droegemeier and Wilhelmson 1985a).

Without some means to trap the upward leakage of wave energy in a stratified atmosphere, gravity waves are incoherent, short-lived phenomena. Three wave-trapping mechanisms were proposed by Crook (1988): 1) the curvature in the velocity profile associated with a low-level jet opposing the wave motion, 2) winds in the mid to upper troposphere opposing wave motion, and 3) a midtropospheric inversion at a height of one-quarter of a vertical wavelength above a surface-based stable layer. All three atmospheric structures support a sudden decrease in the Scorer parameter with height. Crook's analysis of published gravity current-induced bore studies strongly suggested that the low-level jet mechanism was the most frequent way to trap gravity waves and bores, a conclusion that was further supported in the Raman lidar study of Koch et al. (1991).

High-resolution numerical simulations reveal more detailed structure of gravity currents and gravity waves. As illustrated by Droegemeier and Wilhelmson (1985a), generation of wave structure atop the thunderstorm outflow is associated with KH instability. The waves in their study originated at the leading edge of the gravity current and propagated rearward. These findings have been supported in detailed Doppler radar analyses (Mueller and Carbone 1987; Weckwerth and Wakimoto 1991; Ralph et al. 1993). Numerical simulations of gravity currents by Haase and Smith (1989b) show that the quantity $\mu = c_0/c_{gr}$ (where c_0 is the phase speed of long gravity waves propagating on the stable layer of a finite depth and c_{gr} is the speed of the equivalent gravity current in the absence of the stable layer) is one important parameter characterizing the evolution of the gravity current and its associated gravity waves. In the regime of $\mu < 0.7$ (the supercritical regime), the gravity current moves faster than any gravity waves and has a well-defined head structure that is followed by a feeder flow (the cold flow immediately behind the head of the gravity current directed toward the head in a reference frame moving with it). When the value of μ increases to near 0.7, but still within this supercritical regime, undular-type bores may form. When μ is greater than the critical value 0.7 (the subcritical regime corresponding to a deep stable layer), undular bores or solitary waves are spawned by the gravity currents and move ahead of the gravity current. The sec-

ond governing parameter is the Froude number Fr = $\bar{u}/c_*$ (the ratio of the uniform cold-air inflow velocity $\bar{u}$ to the "densimetric" speed $c_* = g\Delta\bar{\theta}d_c/\theta$, where g is the acceleration due to gravity, $\Delta\theta$ is the potential temperature difference between the cold air of the gravity current and the warm air of its environment, d_c is the depth of the gravity current, θ is the potential temperature of the warm air). For large values of Fr, several such solitary waves may form ahead of the gravity current.

Heating or cooling a portion of a simulation domain is a method often used to produce a cold outflow similar in nature to gravity currents (Thorpe et al. 1980; Lin and Smith 1986; Seitter 1986; Raymond and Rotunno 1989). Three pertinent nondimensional numbers were derived and employed by the above authors to depict the behavior of gravity currents and gravity waves. They are, namely, the approximate propagation speed of gravity waves (U_g) resulting from the imposed cooling, the material outflow velocity under constant stratification and no wind shear (U_c), and the opposing ambient wind speed (U). Results from Raymond and Rotunno (1989) indicate that characteristics most resembling a gravity current develop when the ambient flow is supercritical relative to waves ($U > U_g$) but subcritical relative to material outflow ($U < U_c$). Lin and Chun (1991) included ambient wind shear to study the linear and nonlinear responses of the atmosphere to an imposed cooling. They showed that weak ambient opposing flow with strong shear can balance the propagation speed of the cold outflow and make it a steady-state, motionless cold pool instead of a propagating gravity current.

Recently an observed gravity current and its associated gravity waves were reported by Ralph et al. (1993; hereafter referred to as R93). Although it was uncertain whether the observed gravity current originated as a scale-contracted cold front or as a gust front resulting from thunderstorm outflow occurring near the leading edge of the cold front, their study provided unique documentation of gravity waves associated with the gravity current. The combined use of two Doppler sodars and a 45-MHz wind profiler enabled the authors to achieve the incomparable vertical profiling from the surface to nearly 10 km above ground level (AGL) at very high sampling (4 s to 2 min) intervals. Both the gravity current and a variety of gravity waves were clearly documented by combining those data with more conventional meteorological data. One unique feature suggested by the observations was lee-type waves forced by the gravity current acting as an obstacle to the prefrontal low-level inflow (R93). However, it remains to fully understand the origins and structures of the disturbances associated with the gravity current as proposed in their study. The limitations of the observational study include the following.

1) Although three crucial rawinsonde ascents were performed, and unique vertical velocity measurements

were made up to 10-km altitude, no other temperature data were available, and horizontal winds were measured only up to ~500 m.

2) Because only vertical profiles from fixed points were available above ground, only wave periods, not phase speeds or wavelengths, were directly measured. Thus, conclusions regarding wave excitation and ducting mechanisms depended somewhat on inferences based on time to space conversions.

3) A data gap (about 800 m) between sodars (19–476 m AGL) and the wind profiler (>1.2 km) probably prevented measurement of the strongest upward motions within this layer.

4) Without observations from which the Richardson number could be calculated, R93 could not confirm their conclusion that the vertical shear between the cold air below and the warmer air above the gravity current created KH instability.

5) It was difficult to determine which mechanisms were responsible for the trapping of the lee-type waves.

6) The observations did not show any time evolution of the various waves due to the fact that the atmosphere was sampled by nonscanning remote sensing systems.

Although the R93 study provides some of the most complete documentation to date of gravity waves associated with a gravity current, important uncertainties regarding the wave-generation mechanisms and the wave structures remain because of the limitations outlined above. Therefore, numerical simulations were performed in this study to test conclusions derived from the observational analyses. First, the available data are used to prescribe the gravity current's environment as part of the initial conditions of a numerical simulation. These conditions include complex, but real, vertical profiles of stratification and vertical wind shear. The observations of the gravity current itself and of the gravity waves are then used to validate the numerical simulations of these features. Having established in what respects the model produces realistic behavior, the simulations can then be used to test some of the uncertainties remaining from the observational study and to more fully portray both the structure and evolution of gravity waves in this event. Of particular interest are tests of the hypotheses that the head of the gravity current acted as an obstacle to the opposing flow and created trapped lee-type waves and that bores did not develop because the prefrontal stable layer was too shallow. As a whole this study attempts to extend both the documentation and the basic understanding of gravity waves generated by gravity currents in the real atmosphere. Section 2 summarizes the pertinent observations from R93. Section 3 depicts briefly the main features of the model used for the simulations. The simulated gravity currents from control runs with coarse and fine resolutions are described in section 4a, which is followed by further exploration of wave generation

and trapping mechanisms in section 4b. Sensitivity experiments are performed to test the effects of the initial wind profile, the elevated isothermal layer, and the depth and strength of the near-surface stable layer. These results are discussed in section 5, which is followed by a summary and conclusions in section 6.

2. Observational overview

The gravity current investigated in R93 during the Mesogers field experiment in southwestern France occurred in an environment containing a nocturnal inversion and elevated neutral layer. The observational network consisted of two Doppler sodars, a 45-MHz radar wind profiler, a special rawinsonde station, and a mesoscale surface observation network. These systems recorded the passage of an atmospheric discontinuity that was marked by a distinct and abrupt shift in wind direction (southeasterly to northwesterly), large vertical velocities (>1 m s^{-1}), a sharp drop in temperature (3–4 K) up to 1.4 km, and a sudden increase in surface pressure (200 Pa). The disturbance was identified as a gravity current moving to the east at a speed of 10 m s^{-1}.

Figure 1 presents a synthesis of the sodar, rawinsonde, and wind profiler observations of the gravity current. This vertical cross section shows sodar-observed vertical velocities up to an altitude of 0.35 km and radar-observed vertical velocities reaching 3 m s^{-1} above 1.2 km. The updraft of greater than 1 m s^{-1} is confined to altitudes below 3.5 km. Notice that there is a 850-m gap of observation data from about 0.35 to 1.2 km. Although direct evidence of a head on the gravity current did not exist in the data, other observational studies have clearly documented such a feature (e.g., Shapiro et al. 1985; Mueller and Carbone 1987).

A fast Fourier transform (FFT) routine was employed to derive the vertical velocity spectra from the observations. The observed vertical velocities from the wind profiler, as shown in Fig. 6 of R93, were bandpass filtered and waves of two periods were present coincidentally with the passage of the gravity current. One wave with an average period of 14 minutes (Fig. 2b) was trapped below 3.3 km and had no vertical tilt. There is also some indication that a much weaker wave with a 22-min period was present and extended above 3.3 km (Fig. 2a). A careful comparison between Fig. 2a and Fig. 6 of R93 indicates that this wave is not an artifact of the filter. Both waves were strongest at the top of the cold air and lasted for less than one hour at the measurement location. Sodar-detected waves with an average period of 5.5 minutes were found near the surface (strongest at 250 m), extending only 10 km behind the leading edge of the gravity current (Fig. 2c).

A schematic of the observed gravity current in the complex mesoscale environment and its associated gravity waves was constructed by synthesizing the ob-
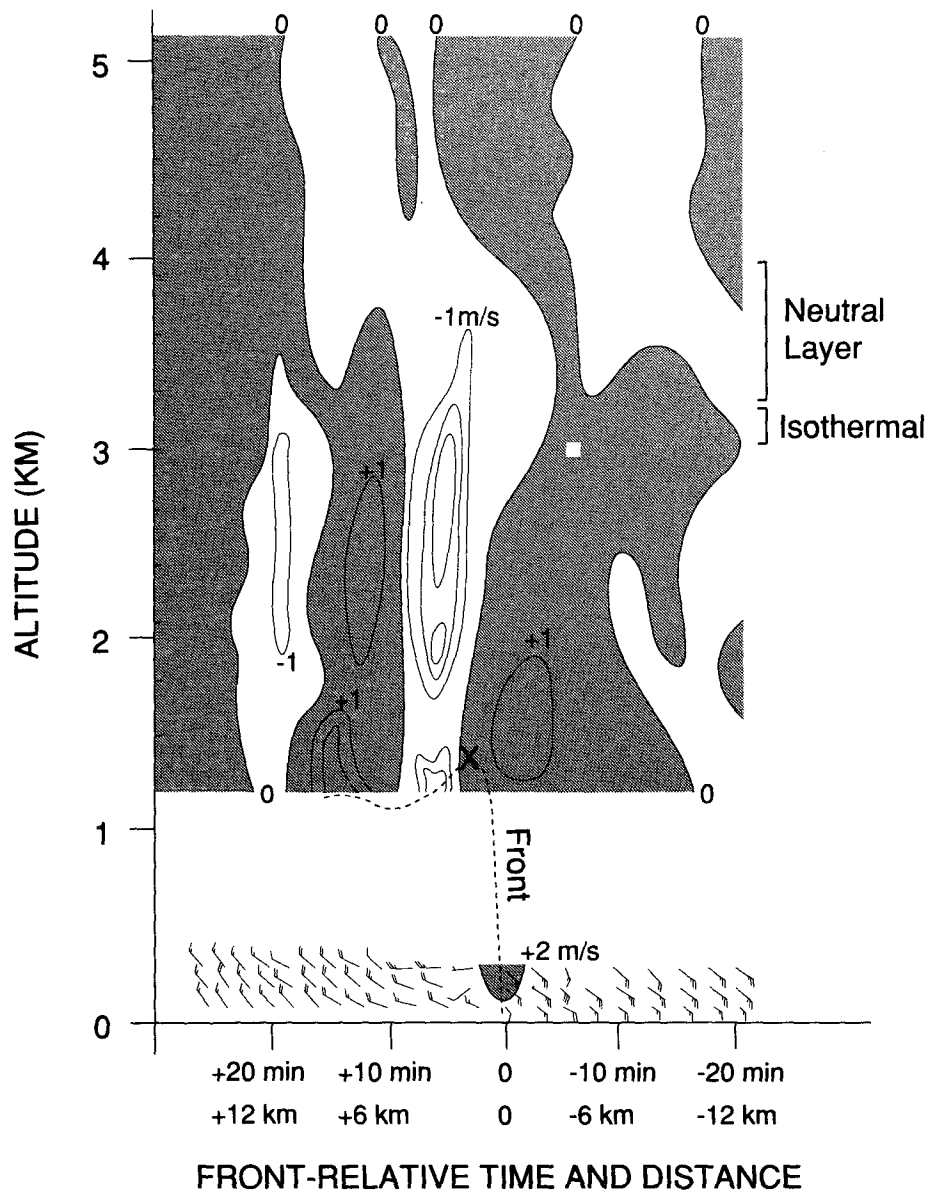
FIG. 1. Synthesis of profiler, sodar, and rawinsonde observations of the gravity current. An observation gap exists between 350 and 1200 m; the sodar-observed vertical velocity is shown below the gap and the radar-observed vertical velocity above (contoured at 1 m s^{-1} intervals with upward motions shaded). The rawinsonde-observed neutral and isothermal layers and depth of the cold air (shown by x) are also marked (from R93).

servational data (Fig. 3). Thus, the detailed vertical structure of the gravity current and the gravity waves excited by the gravity current are well documented. Table 1 summarizes the wave activities occurring within the different regions shown in Fig. 3 as well as the hypothesized wave origins and propagation mechanisms. The primary objectives of the present study are first to generate numerically a gravity current and associated gravity waves that display characteristics as close as possible to the observed ones and second to

test the hypotheses proposed by R93 for the wave origins and propagation mechanisms.

3. The model and its initial conditions

The model used is a two-dimensional, nonhydrostatic, elastic, dry, primitive-equation model (Chen 1991). It uses finite differences and a time-splitting scheme to solve prognostic equations on a staggered grid. Radiative lateral and upper boundary conditions
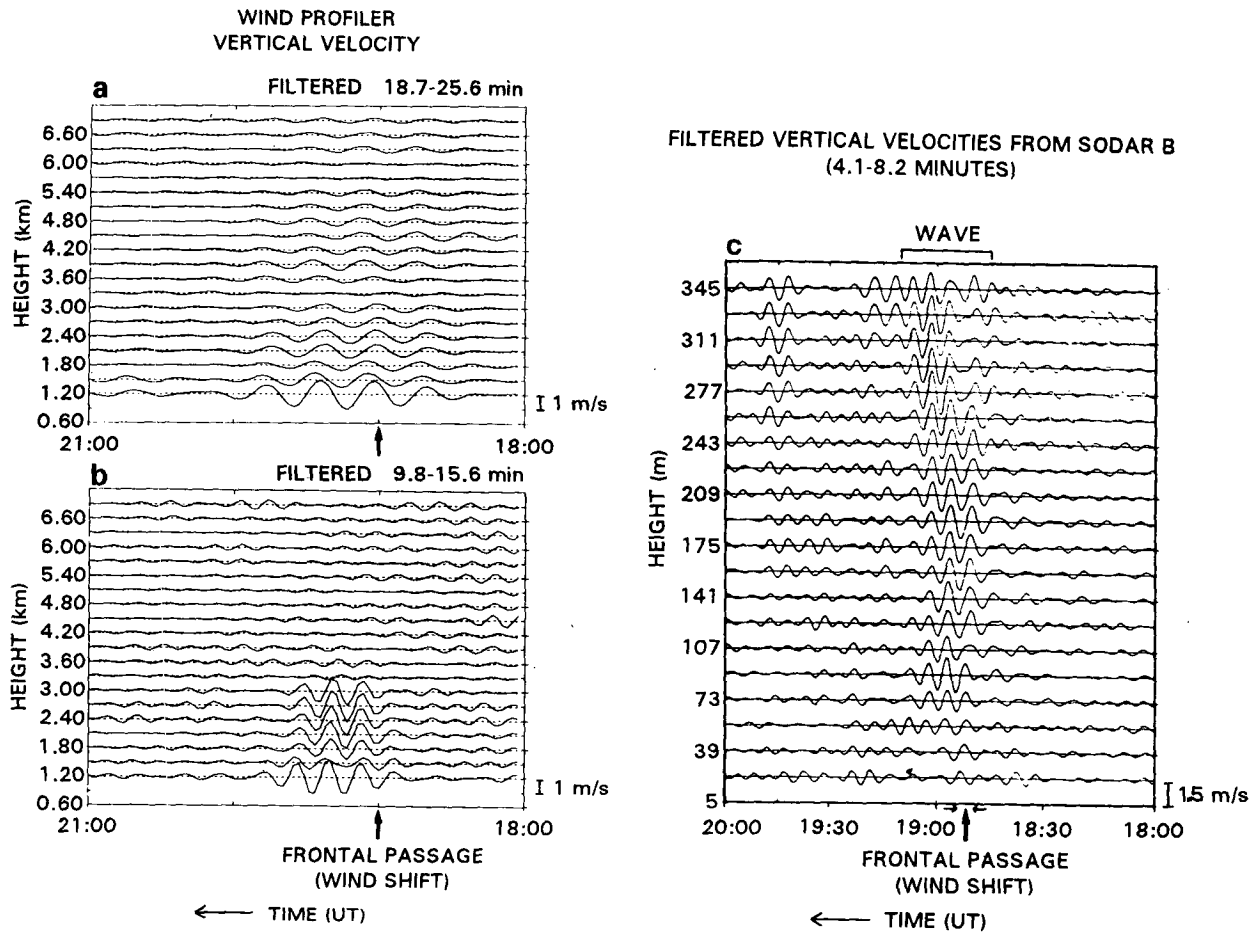
FIG. 2. Bandpass-filtered vertical velocities for waves of three prominent periods observed by (a) and (b) the wind profiler at heights 1.0 < z < 7.2 km and (c) by two sodars at heights below 0.35 km (from R93). The unfiltered data for (a) and (b) are shown in Fig. 6 of R93: the time–height cross section of vertical velocities observed by the wind profiler.

are used to allow gravity wave energy to freely propagate out of the domain. The lower-boundary condition is free slip and no surface friction is considered. Although it is not the best boundary condition, the results from earlier numerical simulations of gravity currents by Haase and Smith (1989a,b) and Seitter (1986) support the choice of the free-slip boundary condition. A fourth-order spatial filter is applied to stabilize the solution. The model also has a conventional first-order turbulence closure scheme (Durran 1986; Clark 1977) for subgrid mixing. Two sets of grid mesh were tried for the simulations. The coarse grid mesh has Δx = 1000 m, Δz = 100 m, with 258 grid points in the horizontal direction and 61 in the vertical. The grid spacing of the fine grid mesh is increased to Δx = 200 m, Δz = 50 m, with 1026 grid points in the horizontal direction and 101 in the vertical. Simulation results discussed in section 4b are from the fine-resolution run only because the coarse grid mesh is unable to resolve most of the wave activity of interest to this case, but

some sensitivity tests were performed on the coarse grid to optimize use of computing resources.

The sounding used to describe the initial environment for the model control runs (Fig. 4) is based on the composite prefrontal sounding presented in R93. Because the sounding times were not ideal, some uncertainty remained regarding the precise environment into which the gravity current propagated, whereas the prefrontal wind profile is well documented and is used here to describe the environmental winds (Fig. 5). An isothermal layer near 3.5 km AGL appeared sometime between 5 hours prior to the passage of the gravity current and a few minutes after its passage. Because the environment of the observed gravity waves contained this isothermal layer, the sounding containing the isothermal layer near 3.5 km AGL (see Fig. 3, reproduced from R93) is used here to define the environmental sounding. However, a test was performed with this layer removed and will be described later. In addition, an inversion 250 m deep near the surface was

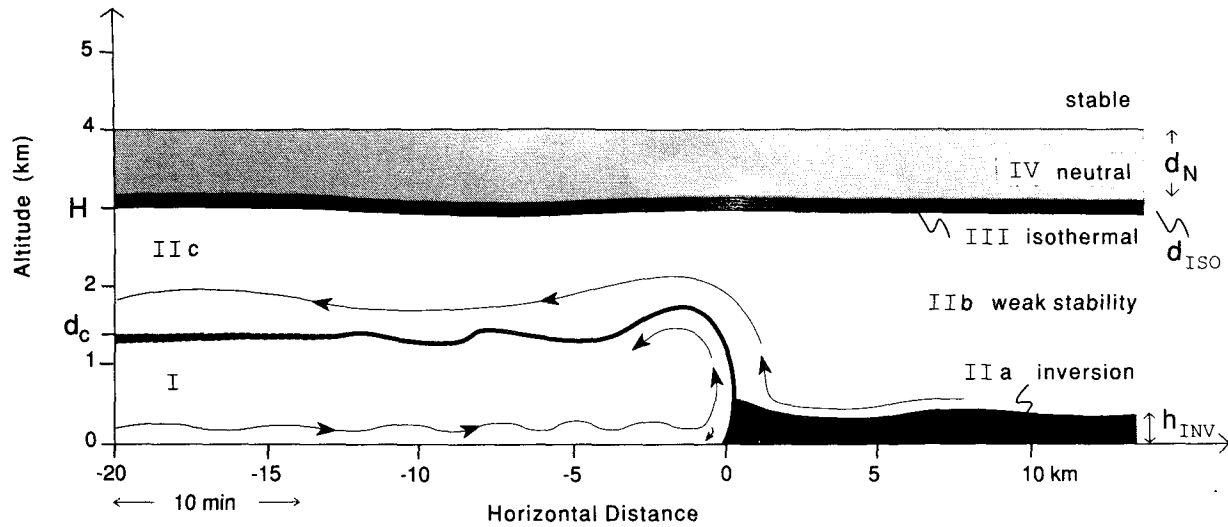## Frontal Environment and Gravity Waves (28 September 1984)

FIG. 3. Schematic of the gravity current, the observed gravity waves, and the local environment. Regions are defined as follows: I, postfrontal cold air ($0-1.4$ km, $d_c = 1.4$ km); IIa, prefrontal radiation inversion ($0-0.3$ km, $h_{INV} = 0.3$ km); IIb, prefrontal air above the radiation inversion ($0.3-3.0$ km); IIc, prefrontal air above the cold postfrontal air ($1.0-3.0$ km); III, a thin elevated isothermal layer or inversion ($3.0-3.3$ km, $d_{ISO} = 0.3$ km); IV, a neutral layer aloft ($3.3-4.0$ km, $d_N = 0.7$ km) (from R93).

also present, above which was a layer of weak static stability up to the isothermal layer near 3.5 km AGL. The depth of the surface-based inversion is changed in sensitivity tests designed to examine the earlier conclusion that it was too shallow to support an undular bore. The initial wind profile (Fig. 5) shows that there is an easterly flow below 1.7 km with the maximum wind speed of 7.5 m s^{-1} near the surface, whereas the wind changes into westerly flow at high levels (above 1.7 km). Except for the thin layers of strong curvature at

low levels, the wind profile is basically composed of two layers of linear shear with a strong curvature point at the interface between the two layers at $z = 3.1$ km.

A strong steady-state heat sink, which is ascribed to the evaporative cooling of precipitation in the subcloud layer (Seitter 1986; Lin and Chun 1991), was incorporated into the model to generate the propagating gravity current. It is located at one-third of the domain width from the left boundary to reduce spurious boundary effects. By trial and error it was determined that a

TABLE 1. Observed gravity waves in the zones defined in Fig. 3.

Zone	Wave existence	Wave period (min)	Wavelength* (km)	Major features	Hypothesized wave origins and propagation mechanisms
I	Yes; 2 waves	(1) 5–5.5 (2) 10–10.5	No calculation No calculation	(1) Extending 10 km behind the gravity current (GC) leading edge, strongest at $z = 250$ m (2) Extending 40 km behind the GC leading edge, above 100 m	(1) Waves propagating downward (2) No discussion
IIa	No	—	—	—	—
IIb	No	—	—	—	—
IIc and Interface of I and IIc	Yes; 2 waves	(3) 14 (4) 22**	(3) 1.8–2.9 (4) 12.5	(3) In the regions from 1.2 to 3.3 km, absence of vertical tilt (trapped) (4) Same as (3) except it lasted for ~1 h.	(3) Shear-induced and trapped waves by the neutral layer (4) Lee-type waves forced by the GC head trapped by the neutral layers at 3.2–4 km
III	No (?)	(5) 44 (?)	No calculation	Anomaly	No discussion
IV	No	—	—	—	—

* The wavelengths were all inferred by R93 based on different assumptions. See section 4b for more discussion.
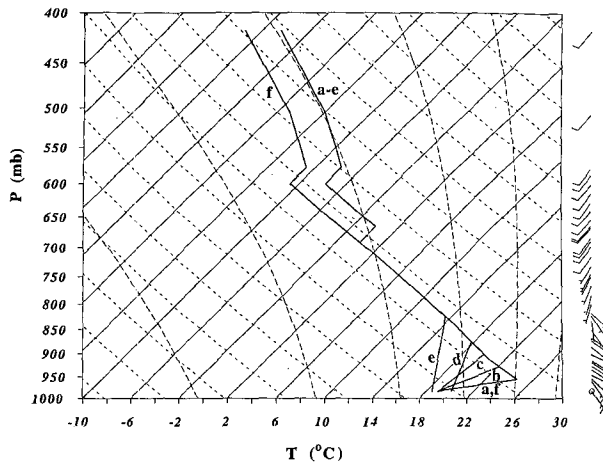** This period was not observed but deduced by R93.

FIG. 4. (a) Initial skew T–$\log p$ sounding for the control runs. This is a prefrontal sounding from Fig. 11 of R93 constructed as explained therein and contains a surface-based inversion of depth $h_{\text{INV}} = 250$ m. Initial soundings for the sensitivity tests, described in sections 5a and 5b, are also included: (b) for test H500; (c) for test H750; (d) for test H1000; (e) for test H1500; and (f) for test NISO.

heat sink 5 km wide and 2.8 km deep, with a constant cooling rate set to 34 K h^{-1} (Fig. 6), generated a gravity current similar to that observed.

4. Results and discussion

a. The gravity current

The model atmosphere's response to the heat sink bears characteristics of a gravity current that moves at the same speed as the observed gravity current ($c_{\text{gr}} = 10$ m s^{-1}). Figure 7 shows the simulated gravity current at model time $t = 1.8$ h with the coarse resolution. The distribution of isentropes (Fig. 7a) indicates that the mean depth of the gravity current is about 1.4 km and that the air immediately behind the front averages 4°C cooler than that before the gravity current up to 1.2 km. These modeled characteristics reproduce those observed in R93 several minutes after the front passed. The greatest temperature contrast across the head of the gravity current reaches 6°C at about the 500-m level in the simulation, which was not resolved by the observations.

A well-defined wind reversal clearly marks the gravity current within the lowest 1 km (Fig. 7b). In a small region at 400–500 m AGL behind the leading edge of the gravity current, the flow is directed toward the leading edge at a speed exceeding 11 m s^{-1}, which is greater than the motion (10 m s^{-1}) of the gravity current. This feature is characteristic of gravity currents. The observed front-normal horizontal winds from the sodar (Fig. 13 in R93) showed flow in excess of 12 m s^{-1} at an altitude of 100 m AGL within about 3 km behind the front. The fact that the modeled maximum post-front horizontal wind speed is at 400–500 m
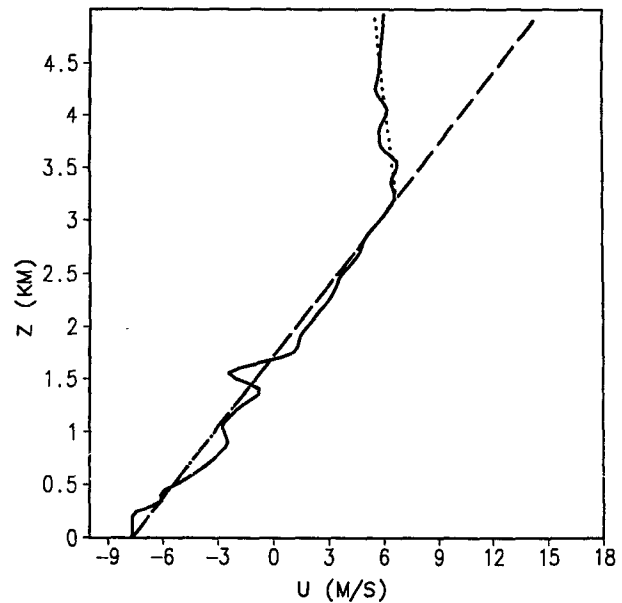

FIG. 5. Initial wind profile for the control runs (solid line). Initial wind profiles for sensitivity tests SP (dotted line) and LS (dashed line) are also shown. Section 5a discusses the two tests. Negative u values indicate easterly flow; positive u values indicate westerly flow.

AGL, while the observed maximum was at 100 m, is likely related to some possible defects of the model configuration. First of all, the structure of the heat sink used for creating the gravity current might be different from the real cooling process in the atmosphere. The free-slip boundary condition and the lack of planetary boundary-layer treatment in the model also could be responsible for this discrepancy. Likewise, the model results also indicate the existence of the inflow (about -7 m s^{-1}) ahead of the front, which agrees with the sodar observations (-7 m s^{-1}), although the model has this maximum at 100 m AGL, while the observations
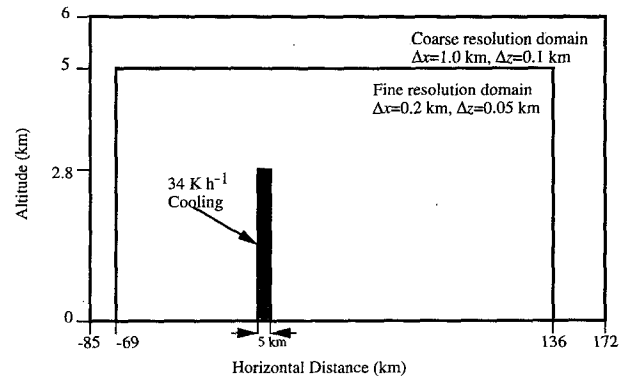

FIG. 6. Schematic diagram of the heat sink incorporated in the model with respect to the simulation domain of the fine resolution (1026 × 101 grid points) embedded in that of the coarse resolution (258 × 61 grid points). The cooling rate of the heat sink = 34 K h^{-1}.
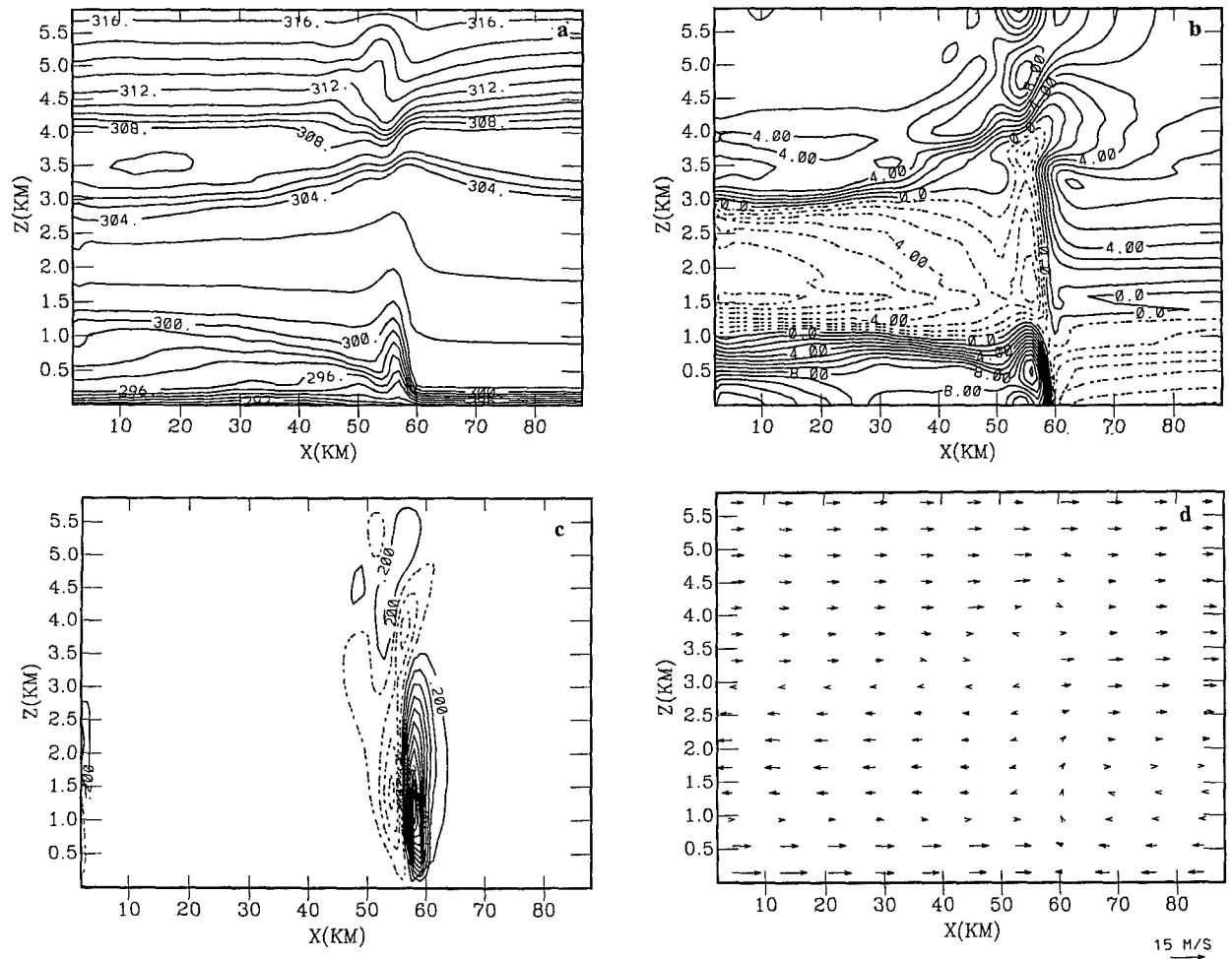
FIG. 7. Simulation results for the control run with the coarse resolution at $t = 1.8$ h: (a) isentropes (K); (b) horizontal wind speed u (m s^{-1}), contoured at 1 m s^{-1} intervals; (c) vertical velocity w (m s^{-1}), contoured at 0.4 m s^{-1} intervals; (d) wind vectors.

had it at 200 m AGL. The strong easterly flow is elevated by the intrusion of the cold air, resulting in significant vertical shear of horizontal wind at the interface between the cold air and its environment. The vertical shear at the top of the gravity current is 14 m s^{-1} (0.5 km)$^{-1}$ = 2.8 × 10^{-2} s^{-1}. This shear is considered to be the major mechanism for KH waves appearing later in this region (further discussions in section 4b).

In the simulation, the gravity current causes air parcels of the opposing inflow at levels below 1 km to decelerate in front of the gravity current head and induces corresponding patterns of divergence–convergence and vertical motions. Figure 7c shows that an upward motion exists and is centered on the upstream side of the leading edge of the gravity current, with values increasing from zero at the surface to greater than 3 m s^{-1} at about 300 m, as observed. In the simulation the strong vertical motion produced by the gravity current is confined to the layers below 3.5 km, in

close agreement with that deduced by R93 from the wind-profiler vertical velocity data (Fig. 1), however, the observed vertical motions were weaker in the 1.5–2.0 km layer. It is possible that three-dimensional structures, such as those illustrated in Simpson (1987), were present in the observed event but could not be captured in two-dimensional simulations. The vertical extent of the updraft was suggested by R93 to be limited by the neutral layer just below 700 mb (curve a of Fig. 4; also see Fig. 11 of R93), a behavior consistent with the wind profiler observations (Fig. 6 of R93) and our model results (Fig. 7c). This is consistent with the fact that deep convection did not develop from the lifting along the gravity current head because the level of free convection was not reached. Although the simulation produces a maximum updraft of 4.5 m s^{-1} that is stronger than the observed maximum of 3 m s^{-1} (Fig. 1), the simulated maximum is at an altitude within the observational gap near 1 km. The maximum vertical

velocity retains this value throughout the second hour of the simulation after it reaches a quasi-steady state. As can be inferred from the u-component and wind vector fields, near the head of the gravity current, strong convergence exists below about 1 km and divergence from about 1.5 to 3.5 km.

The simulation with fine resolution ($\Delta x = 200$ m, $\Delta z = 50$ m) produces nearly the same general features of the gravity current as in the coarse resolution except that the maximum vertical velocity forced by the intruding gravity current increases to 6.3 m s^{-1} (Fig. 8). This value is twice the observed maximum value. This disagreement can still be attributed to the aforementioned observation gap, although it is also possible that the 2-min averaging by the wind profiler misrepresented the actual maximum updraft speeds. It is possible that the 2-min averaging, which corresponds to 1.2-km horizontal averaging based on the gravity current's 10 m s^{-1} propagation, is more representative of the 1.0-km resolution run than the 0.2-km horizontal resolution run. One feature common to gravity currents,

that is, the overturning circulation within the gravity current head, is also captured by the simulation. The most significant difference between the two simulation results is that in the fine-resolution run, waves distort both the upper boundary of the gravity current and the regions above the cold air behind the gravity current head. These features are explored in the following section.

b. Gravity waves

Although the major characteristics of the gravity current are well simulated by the coarse-resolution run, the only major wave activity simulated is a vertically propagating hydrostatic wave forced by the well-defined gravity current head, whereas the fine-resolution simulation produces several other waves as well. These waves are summarized in Table 2 on the same zonewise basis as Table 1 in order to compare with the observations. Each wave is represented by a contour of potential temperature because waves are clearly seen in
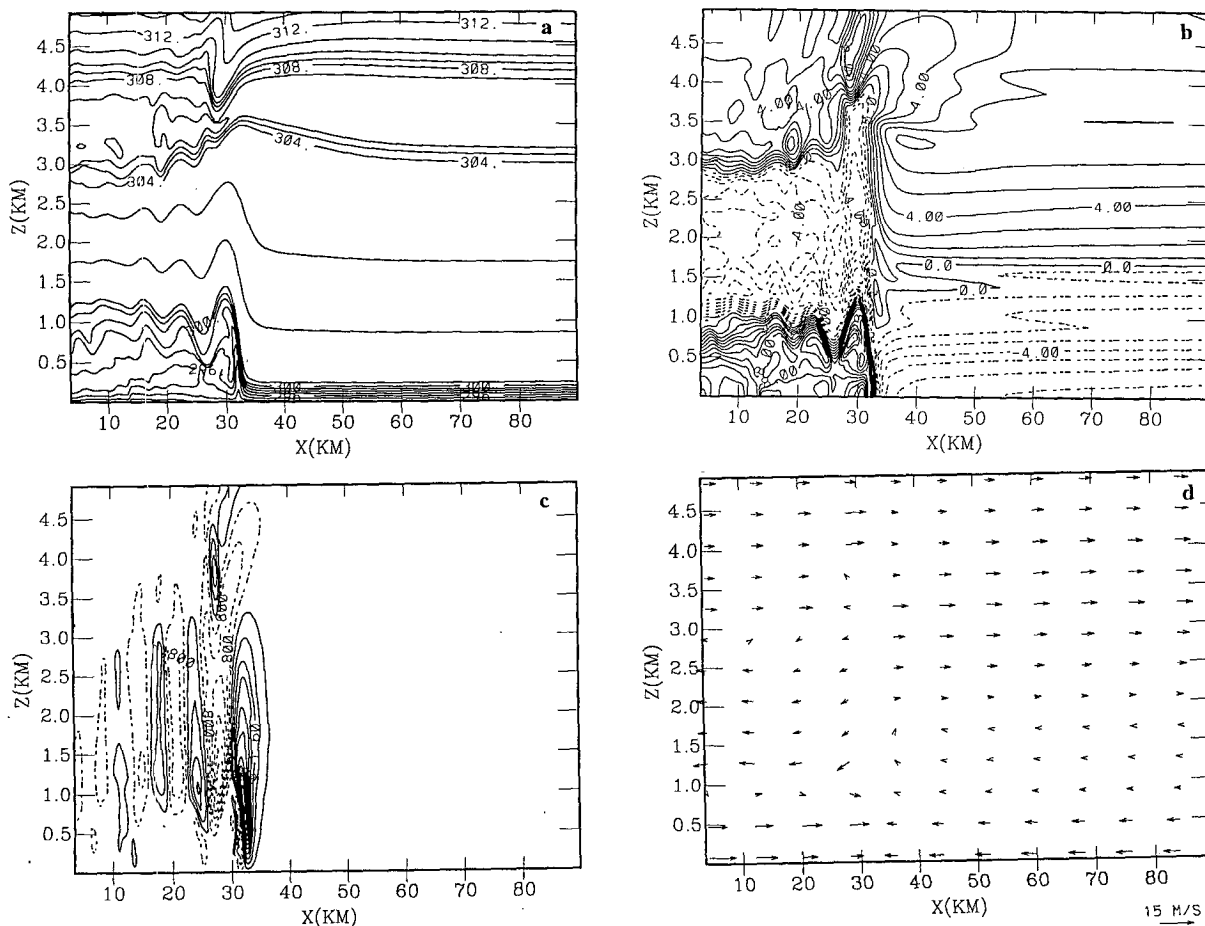

FIG. 8. Simulation results for the control run with the fine resolution at $t = 1.0$ h: (a) isentropes (K); (b) horizontal wind speed u (m s^{-1}), contoured at 1 m s^{-1} intervals; (c) vertical velocity w (m s^{-1}), contoured at 0.4 m s^{-1} intervals; (d) wind vectors.

TABLE 2. Simulated gravity waves in the zones defined in Fig. 3.

Zone	Wave existence	Wave period (min)	Wavelength (km)	Major features	Wave origin and propagation mechanism
I	Yes	(1) 15	(1) 2.2–2.4	(1) Extending 10–40 km into the cold air; $z = 100$–800 m; $\theta = 294$–298 K; developing from $t = 1.2$ h	(1) Shear induced (KH waves)
IIa	No	—	—	—	—
IIb	No	—	—	—	—
IIc and Interface of I and IIc	Yes; 3 waves	(2) 11 (3) 12 (4) 20–23	(2) 6.4 (3) 8 (4) 2.7	(2) Behind the GC head; absence of vertical tilt; strongest above the cold air; $\theta = 302$ K (3) Above the GC head; $\theta = 302$ K; absence of vertical tilt (4) About 20 km behind the GC head; developing from wave (3) at $t = 1.2$ h; $\theta = 300$ K	(2) Forced by the GC head and trapped by the curvature aloft associated with the low opposing inflow and the isothermal layer (3) Same as wave (2) (4) Shear induced (KH waves)
III	Yes	(5) 8	6	$\theta = 306$ K	Vertically propagating
IV	Yes	(5) 8	6	$\theta = 306$ K	Vertically propagating

isentropes. Parameter m^2 and the Richardson number Ri are calculated so that the possible mechanisms for wave origin and propagation can be investigated. The equation determining the vertical wave number (m) is

$$m^2 = \frac{N^2}{(u - c)^2} - \frac{\partial^2 u/\partial z^2}{u - c} - k^2 = l^2 - k^2, \quad (1)$$

where $u - c$ is the horizontal wind relative to the propagating speed of the gravity wave (c); N is the Brunt–Väisälä frequency; $\partial^2 u/\partial z^2$ is the curvature in the wind profile; k is the horizontal wavenumber; z is the altitude; and l is the Scorer parameter

$$l^2 = \frac{N^2}{(u - c)^2} - \frac{\partial^2 u/\partial z^2}{u - c}. \quad (2)$$

On the basis of the Goldstein–Taylor equation, a wave with $m^2 > 0$ can propagate vertically; a wave with $m^2 < 0$ is evanescent because its amplitude decays exponentially with height. The Richardson number is determined as

$$\text{Ri} = \frac{N^2}{(\partial u/\partial z)^2}. \quad (3)$$

The Miles theorem (Miles 1961) states that Ri < 0.25 is the necessary condition for the KH instability.

It appears in Fig. 8 that the well-defined gravity current head acts as an obstacle that generates gravity waves (waves 2 and 3 in Table 2) as it encounters the surrounding environment. Time evolution of these waves for the first hour of integration is shown in Figs. 9a and 9b. As an air parcel within the inflow region approaches the leading edge of the gravity current, it is displaced upward until reaching the crest of the gravity current head and then descends the lee side of the gravity current head. In an environment conducive to trapping of gravity wave energy, the upward and down-ward displacement can excite a train of trapped lee-type waves. This behavior is suggested by following the 302 K isentrope in Fig. 9a as it is perturbed from its initial state. Three or four distinct undulations are found trailing the head of the gravity current and have a wavelength of ~6.4 km (Fig. 9b). Similar undulations are found in the layer between 0.5 and 3.0 km. Vertically oriented phase lines, a characteristic of trapped waves, are clearly present in this layer. This structure closely resembles the one documented by observations both in terms of the lack of phase tilt and the vertical extent of the undular perturbations (Figs. 1 and 2). Also in good agreement with the observations is the sharp negative peak behind the gravity current head (Fig. 6 of R93), which also had been observed by Doviak and Ge (1984). These results represent strong validation of this aspect of the simulation, indicating that the model can be used to further test the wave-generation hypothesis. According to this trapped lee-wave hypothesis, the wave should be motionless relative to the gravity current head. This behavior could not be determined from the observations but is present in computer animation of the simulation, in which these waves travel at 8.8–10.7 m s^{-1}. The gravity current propagation speed is 10.0 m s^{-1}.

Figure 10 shows the distribution of the square of the vertical wavenumber (m^2) at the initial time in the control run. The x-axis scale is chosen to highlight small changes in m^2, which represent the large-scale conditions affecting wave propagation. The 6.4-km horizontal wavelength and 10 m s^{-1} phase speed are used in the above calculation, but major features in the m^2 distribution persist for varying phase speeds from 8.8 to 10.7 m s^{-1} for both wave 2 and wave 3. The atmosphere ahead of the gravity current is not very much disturbed by the intrusion of the cold air and basically retains this structure in the distribution of m^2 during the 2-h simulation. The m^2 distribution
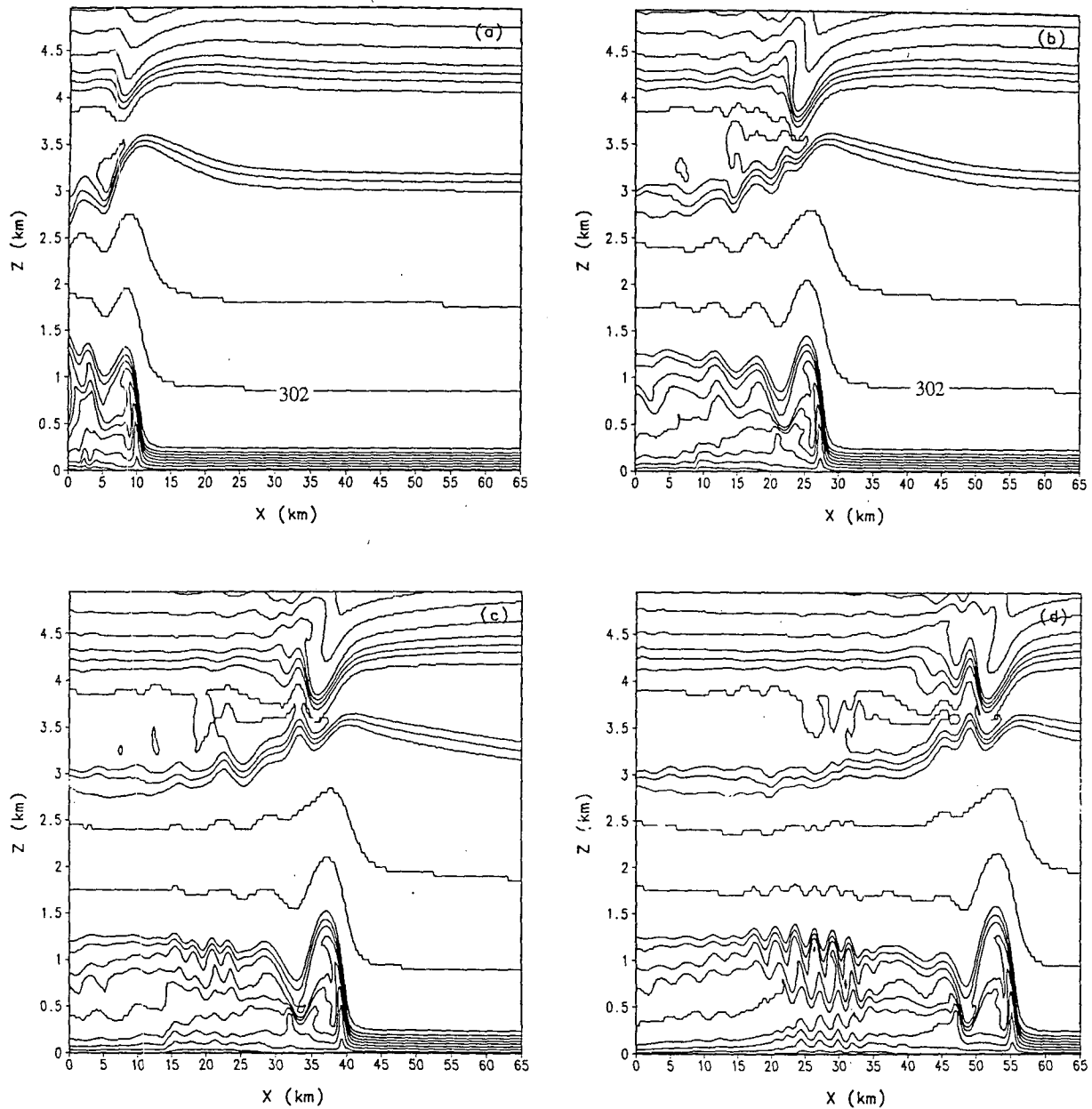
FIG. 9. Distribution of isentropes for the control run with the fine resolution (contoured at intervals of 1 K) at (a) $t = 0.5$ h, (b) $t = 1.0$ h, (c) $t = 1.37$ h, and (d) $t = 1.75$ h.

shown in Fig. 10 can be considered to be composed of three pairs of lower and upper layers (Table 3) based on the associated wave activities. For each of the three pairs, layer-averaged m^2 is positive and negative for the lower and upper layers, respectively, which makes it possible for internal wave modes to exist in the lower layers. Furthermore, the necessary condition for the existence of trapped lee waves for the two-layer problem is that

$$l_L^2 - l_U^2 > \frac{\pi^2}{4H^2}, \qquad (4)$$

where l_L and l_U are the Scorer parameters in the lower and upper layers, respectively, and H is the depth of the lower layer (Scorer 1949). This condition is not met for the first two pairs in Table 3, but the inequality (4) is well satisfied for the third-layer pair with the left-hand side nearly one order of magnitude greater than
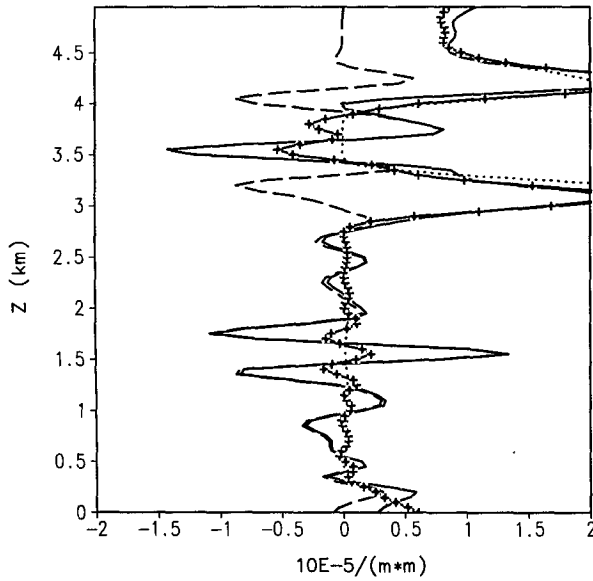
FIG. 10. Profile of the square of the vertical wavenumber m^2 (solid line) at the initial time for the control run. The dashed and dotted lines are contributions of the curvature term $-u''/(u-c)$ and the term $N^2/(u-c)^2$, respectively. The crossed line is the m^2 profile for test SP as discussed in section 5a.

the right-hand side. Additional calculation reveals that the upper layer of the third-layer pair still works well (with the left-hand side more than one order of magnitude greater than the right-hand side) for wave trapping when the lower layer extends down to 1.0 km. Thus the above analysis attests to the existence of the wave-trapping mechanism and strongly supports the interpretation by R93 that the waves observed within the layer between 1.2 and 3 km were trapped lee-type waves. Also shown in Fig. 10 are contributing terms to m^2 from the curvature and the term related to the Brunt–Väisälä frequency. It was mentioned by R93 that the elevated neutral layer serves as a possible mechanism to trap the waves, but it seems in Fig. 10 that the curvature of the initial wind profile aloft also plays an important role as the trapping mechanism. Sensitivity tests were performed to improve understanding of this issue and are discussed in section 5a.

Part of the wave energy can still propagate vertically up to 3.5–4 km and manifest itself as waves in the isothermal and the neutral layer there (wave 5 in Table 2), but the wave period (8 min) differs from that in R93 (22 min), in which the period was estimated based on several assumptions stated therein.

There are several issues that need to be addressed regarding the applicability of Scorer's theory to the current case. First of all, Scorer's work (1949) studied very restricted vertical variation of both the stability and the wind speed. Sawyer (1960), however, extended Scorer's earlier work by simulating lee waves for eight observed cases. His results show that lee

waves of which the amplitudes decrease with height were clearly related to a substantial drop in the Scorer parameter with height. The flow patterns for individual cases varied widely, but this general characteristic was retained, which is also true for the current case. Second, the roughly 2 m s^{-1} perturbation winds are nearly of the same order as the 4–6 m s^{-1} background flow for the current case, and thus the small amplitude assumption of Scorer's theory is violated. However, several earlier studies have successfully shown favorable comparisons between the linear theory and observations even when the wave amplitude was fairly large, for example, Holmboe and Klieforth's (1957) report on the Sierra Wave project, several aircraft-observed cases in Foldvik (1962), and Vergeiner and Lilly (1970). This suggests that the theory is not overly sensitive to this assumption. Moreover, the wind-tunnel simulation of lee waves by Lin and Binder (1967) clearly shows the simulated lee waves in flows with Froude numbers ranging from 0.234 to 0.214, in which case the flow is highly nonlinear. The lower layer of their two-layer model had large stability, which caused large decrease in the Scorer parameter with height given the constant wind speed. Lastly, the theory was derived from steady-state conditions, but in reality the waves will evolve over time. This issue was explored in Queney et al. (1960), where it was established that trapped lee waves can change structure on timescales governed by their group velocity and horizontal wavelength. The timescale for an entire horizontal wavelength to change should be under 1 hour in many cases. This is verified in simulations by Foldvik and Wurtele (1967). More recently Lott and Teitelbaum (1993) found the same result when considering how long it would take to change a single vertical wavelength of order the depth of the troposphere. Thus changes in the trapped waves over 0.75 hours in the current numerical simulations (Fig. 9) are consistent with the earlier studies.

As the model is integrated to $t = 1.27$ h, waves of shorter wavelengths begin to develop at the interface

TABLE 3. Vertically averaged values of l^2 for each significant layer of the initial atmospheric structure of the control run.

Layer pair	Layer height (m) Lower Upper	$\bar{l}^2_{lower} - \bar{l}^2_{upper}$ ($\times 10^{-5}$ m^{-2})	$\dfrac{\pi^2}{4H^2}$ ($\times 10^{-5}$ m^{-2})
I	0–500 500–950	0.494	0.99
II	950–1300 1300–1800	0.535	2.0
III	1800–3400 3400–4050	0.690	0.096

* The bar over l^2 indicates that the square of the Scorer parameter is averaged vertically for each layer.
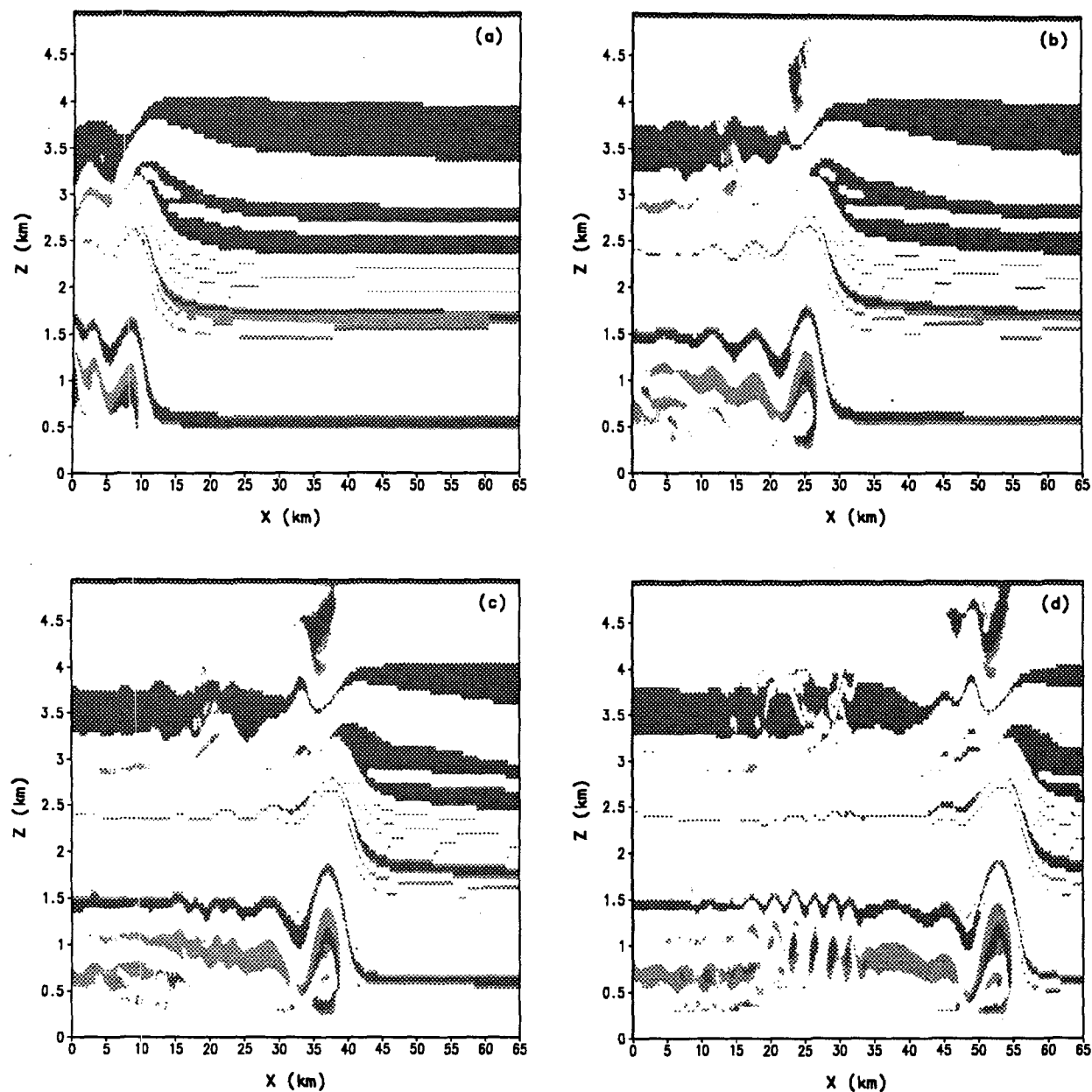
Fig. 11. Distribution of Richardson number for the fine-resolution run with regions of < 0.25 (light gray shaded) and regions of Ri < 0 (dark gray shaded) at (a) $t = 0.5$ h, (b) $t = 1.0$ h, (c) $t = 1.37$ h, and (d) $t = 1.75$ h.

between zone IIc and zone I and are well developed by $t = 1.37$ h. Waves 2 and 3 are evident at this time only in the region at $z = 1$ km about 20 km extending behind the leading edge of the gravity current (Fig. 9c). Also shown is the evolution of the Richardson number distribution (Fig. 11). At $t = 1.0$ h the area of the light-gray-shaded region below 1.5 km is about 11 km^2. The area increases to about 15 km^2 at $t = 1.37$ h when the short waves are becoming evident. It seems that the shorter waves do not develop either until the regions of

possible dynamic instability get to a certain size or the waves have had enough time to grow to significant amplitudes. The short waves are generated in the region of Ri < 0.25 collocated with regions of strong vertical shear between the prefrontal easterly flow forced above the gravity current and westerly flow of the cold air consisting of the gravity current. Thus, it can be inferred that the main cause for the waves is shear instability or thus the waves are shear-induced KH waves. It seems from Fig. 11d that young short waves develop

about 22 km behind the leading edge of the gravity current and then propagate rearward relative to the gravity current. They magnify while propagating, as evidenced by the increase in their amplitude. After the KH instability grows, the regions of Ri < 0.25 become enhanced and focused into smaller scales by the short KH waves (Figs. 11d). The KH waves act to modify the shape of the region of low Ri and the values of Ri within it, probably through deformations associated with the KH waves. These changes are likely related to earlier observations (e.g., Fig. 2.18 of Gossard 1990) and theory (e.g., Maslowe 1973) that showed KH waves on one scale can create much smaller layers on which KH instability with much smaller wavelengths can then grow.

The simulated wavelengths (2.2–2.7 km) and phase speeds (2.0–2.6 m s^{-1}) are in close agreement with the values estimated from the observations (1.8–2.9 km and 2.1–3.4 m s^{-1}, respectively), but even these small differences cause the simulated wave periods for wave 4 (20–23 min) to diverge from the observed ones (14 min). At $t = 1.75$ h wave 1 occurs in a layer that appears to be centered near 0.1–0.8-km altitude and x = 15–35 km in the domain (Fig. 9d). This indicates that the KH instability perturbs not only the layer at the interface and above but also the layers below.

It is of interest to relate the simulated gravity current and its associated waves to the study of Raymond and Rotunno (1989). Quantitative calculation of the ratio of the approximate propagating speed of gravity waves to the material outflow velocity based on Eq. (20) in their paper is found impossible for the present case since the wind field and stratification are far from being uniform as required. The speeds of the gravity waves and the gravity current from the simulation are used instead to obtain that ratio. The ratios, ranging from 0.18 to 1 for the waves of different wavelengths from the simulation, indicate that the imposed cooling produces a strong gravity current that advances faster than the associated gravity waves. The strongest upward motion occurs just upstream of the cooled region in our simulations (Fig. 7), consistent with their analyses (Fig. 10 of Raymond and Rotunno 1989).

In summary, the simulations of the gravity waves associated with the gravity current and wave generation and propagation mechanisms presented thus far exhibit very good agreement with the observations, although some uncertainty remains concerning details of the KH waves. Nevertheless, further examination of the effect that the initial wind profile has on the wave-trapping mechanism is needed since an important contribution to m^2 is partially from the curvature term (Fig. 10). R93 suggested that the neutral layer was important in trapping wave energy, but the curvature of the wind profile had an uncertain contribution to the wave trapping; however, the observations did not allow profiles of the Scorer parameter and its two contributing terms to be calculated.

5. Sensitivity tests

Because of the good agreement with the observations of the simulated gravity current and its associated gravity waves, the model is used here to more thoroughly test the conclusions concerning the wave-trapping mechanism that led to the existence of the trapped lee-type waves and the conclusion that the prefrontal surface inversion was insufficiently deep to allow for the generation of a bore. These checks are performed by varying the appropriate conditions within the model.

a. Wave-trapping mechanisms

As mentioned above, Crook (1988) proposed three possible wave-trapping mechanisms for short-period (~10 min) gravity waves on a layer of high stability near the ground. For the first mechanism, he showed that the curvature above the low-level jet can produce a layer of negative Scorer parameter. Three different initial wind profiles, designated as SP (smoothed profile), LS (linear shear), and NW (no wind) in Table 4, were examined in the current study to test this wave-trapping mechanism.

The isentropes at $t = 1$ h for the variable wind profile tests shown in Figs. 12b, 12c, and 12d should be compared with those for the control run (Fig. 12a). When the environmental wind profile is modified so as to eliminate small variations that create curvature at low levels but retain the significant curvature near 3.1 km AGL (the dotted line in Fig. 5), the lee-type waves remain essentially unchanged (Fig. 12b). The smoothed m^2 profile for test SP (the crossed line in Fig. 10) does not contain large changes below 3 km, which also indicates that the small features in the wind profile for the control run that create large curvature at low levels (Fig. 10) mask the larger-scale wind shears that do have an important impact on gravity wave vertical propagation. When the curvature is removed from the

TABLE 4. List of sensitivity tests and the control run (CR).

Test	Initial wind profile	Depth of the near-surface stable layer (m)	Existence of the isothermal layer
CR	Observed	250	Yes
SP	Smoothed*	250	Yes
LS	Linear shear**	250	Yes
NW	No wind	250	Yes
NISO	Smoothed	250	No
H500	Smoothed	500	Yes
H750	Smoothed	750	Yes
H1000	Smoothed	1000	Yes
H1500	Smoothed	1500	Yes

* The smoothed wind profile for test SP is composed of two layers of linear shear with the only strong curvature point at $z = 3.1$ km, as shown by the dotted line in Fig. 5.

** The initial wind profile for test LS is a whole layer of linear shear but keeping the low-level opposing inflow, as shown by the dashed line in Fig. 5.
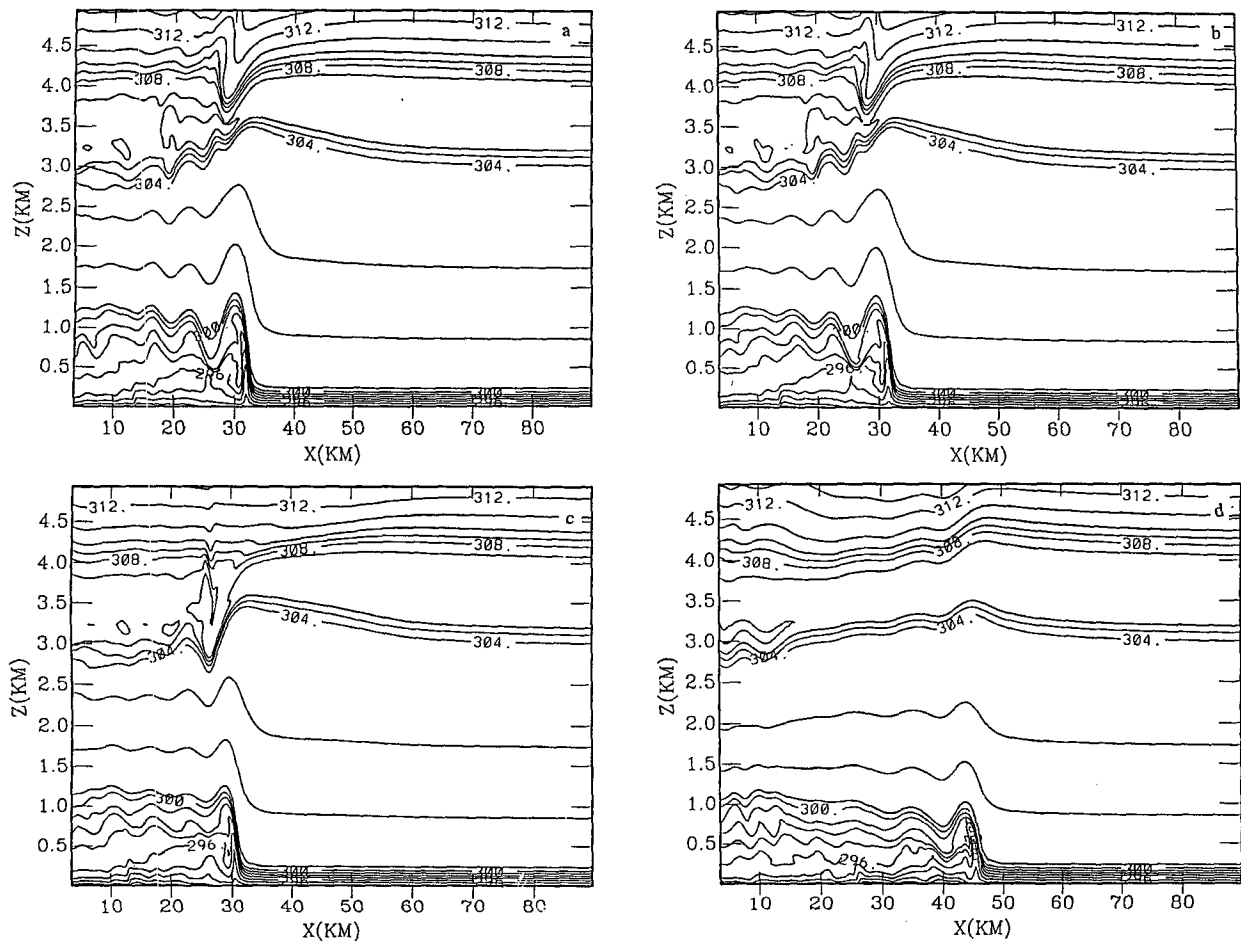
FIG. 12. Isentropes (K) with the fine resolution at $t = 1$ h for (a) the control run (CR); (b) the test with the smoothed wind profile (SP; the dotted line in Fig. 5); (c) the test with the linear shear (LS; the dashed line in Fig. 5); (d) no initial wind (NW) test.

entire wind profile (the dashed line in Fig. 5) but the low-altitude opposing-flow is retained, the wave amplitude is significantly reduced (Fig. 12c). These results lend further support for the argument made in section 4b based on the examination of the m^2 profiles that the curvature aloft (near 3.1 km) is important for wave trapping. Finally, when the environmental wind is set to zero, both the curvature and the low-altitude opposing flow are removed, resulting in even weaker waves and a faster gravity current propagation speed (Fig. 12d). These simulations confirm that the curvature aloft in the wind profile has an important effect on wave trapping in this case, a conclusion consistent with the results from other cases studied by Crook (1988) and the strong bore case observed by Koch et al. (1991).[1]

Nevertheless, the observed coincidence of the sudden weakening of wave amplitudes with the existence of the isothermal layer above 3.3 km, as well as the dominance in the m^2 profile by the contribution from the term $N^2/(u - c)^2$ within the isothermal layer, suggest that the isothermal layer may contribute significantly to trapping the waves. The roles of the isothermal layer in wave trapping is revealed by the results of a sensitivity test (NISO), in which the isothermal layer at about 3.4–3.7 km was removed, but the same lapse rate as that for the control run was maintained elsewhere in the initial sounding (profile f in Fig. 4). The initial wind profile was the smoothed profile, as in test SP, since it retains the major features of the initial wind

---

[1] It is interesting to note that the increase in gravity current propagation speed from 10.0 m s^{-1} with opposing flow to 13.3 m s^{-1} without opposing flow is consistent with the study by Simpson and Britter (1980). Their study concluded that the ground-relative gravity

current propagation speed is reduced by approximately 0.6 times the speed of the front-normal opposing flow, which in our case averages 4.5 m s^{-1} over the depth of the simulated gravity current. Accounting for this headwind effect produces a 2.7 m s^{-1} change in propagation speed, which is in close agreement with the simulated 3.3 m s^{-1} change.

field shown above to contribute to wave trapping. Removing the isothermal layer at 3.4–3.7 km in the initial sounding significantly modifies the wave behavior (Fig. 13). The wavelength is reduced to about 2–4 km in the lower layer, which, as shown in Fig. 14, causes m^2 to be significantly different from l^2 [recall Eq. (1)]. The entire negative m^2 layer from 0.3 to 4 km indicates that the wave is evanescent in this layer. Waves are forced first by the gravity current head and then shortened and strengthened by the shear instability at the interface of cold and warm air, as evidenced by the tilt in the phase lines of the waves near the interface (1.0–1.5 km) in Fig. 13. Amplitudes of the waves decrease with height because $m^2 < 0$ and are strongly depressed by the strong negative value of m^2 related to the strong curvature aloft. There is no tilt in the phase line when the waves become evanescent and away from the wave source region, as expected. It is apparent by comparing the crossed lines in Fig. 10 and Fig. 14 (notice that the x-axis scales are different) that the isothermal layer helps to trap the wave energy in two ways: 1) making the horizontal wavelength long enough ($m^2 > 0$) so that the waves can propagate in the wave duct and 2) causing a strong positive m^2 layer just below the negative m^2 associated with the strong curvature aloft in order for wave activities to be clearly seen until just below the layer of negative m^2 (layer pair III in Table 3). Thus the elevated isothermal layer and the curvature collocated act in concert to maintain the trapped lee-type waves.

b. Bore generation and the near-surface stable layer

In agreement with the observations in R93, the simulation results show no evidence of a bore propagating ahead of the gravity current, even though the gravity current is entering into an environment with conditions
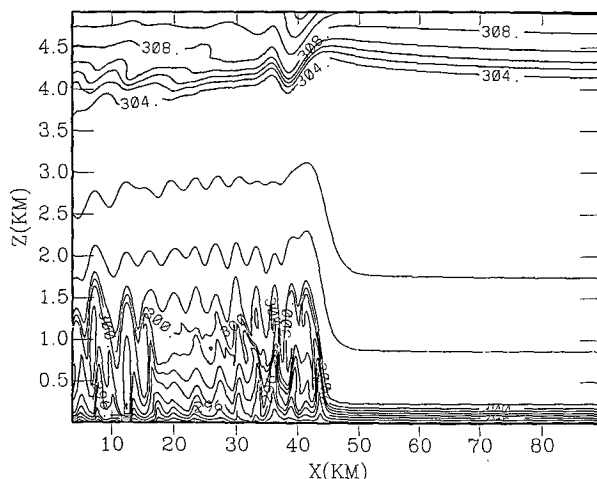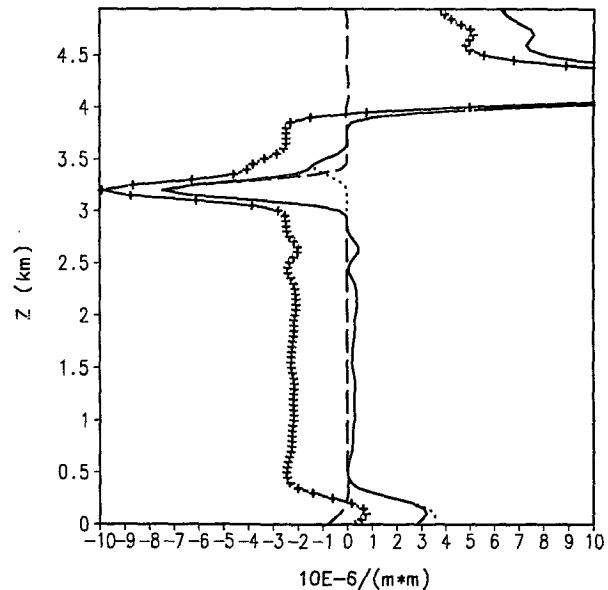

FIG. 14. Profile of the square of the Scorer parameter l^2 (solid line) at the initial time for the NISO test. The dashed and dotted lines are contributions of the curvature term $-u''/(u - c)$ and term $N^2/(u - c)^2$, respectively. The crossed line is the m^2 profile for the 4-km wavelength wave, but the major characteristics in distribution of m^2 are retained for the 2-km wave.

often considered conducive to bore generation, that is, the low-level stability and low-level jet together with the curvature aloft (e.g., Doviak and Ge 1984; Simpson 1987; Crook 1988; Koch et al. 1991). In the observational paper it was concluded that the stable layer near the surface was not deep enough for a bore to develop. Sensitivity tests were performed in the current study to test this hypothesis by increasing the depth of the low-altitude stable layer using the coarse-resolution model.

It is desirable to make the changes to the initial sounding as simple as possible in these experiments. Therefore, the depth of the near-surface stable layer was increased from 250 m for the control run to 500, 750, 1000, and 1500 m for tests H500, H750, H1000, and H1500, respectively, with the surface temperature kept nearly constant, while the temperature at the top of the layer was taken as the temperature at that level in the initial sounding for the control run (Fig. 4 and Table 4). It is shown in Fig. 15 that there is a tendency for a borelike disturbance to develop and for the gravity current to weaken as the depth of the stable layer increases. The propagating speed of the gravity current c_{gr} and the leading wave disturbance c_{gw}, the stability of the low stable layer represented by the Brunt–Väisälä frequency N, and the maximum vertical velocity associated with the disturbance are listed in Table 5 for the four tests, as well as for the control run. Unlike in the control run, the wave disturbance is moving faster than its parent gravity current in each of the simulations with a deeper stable layer. As the stability of the near-

FIG. 13. Isentropes (K) at $t = 1.25$ h for sensitivity test NISO as described in section 5a.

TABLE 5. Results from the sensitivity tests on the depth of the low stable layer compared with the control run (CR).

Test	Height (H) (m)	N (s^{-1})	$c_0 = 2NH/\pi$ ($m\ s^{-1}$)	$\mu = c_0/c_{gr}$ ($c_{gr} = 12\ m\ s^{-1}$)	c_{gr}/c_{gw} ($m\ s^{-1}/m\ s^{-1}$)	w_{max} ($m\ s^{-1}$)
CR	250	0.0327	5.2	0.43	8.8–10.2/10	4.5
H500	500	0.0231	7.4	0.62	7.2/10.3	3.0
H750	750	0.0191	9.1	0.76	5.6/10.2	2.3
H1000	1000	0.0157	10.0	0.83	4.0/11.0	1.7
H1500	1500	0.0147	14.0	1.2	3.9/11.7	0.69

surface stable layer decreases due to increasing its depth, the strength of the disturbance decreases, as evidenced by the reduced maximum vertical velocity (w_{max}). This presumably results from the wave energy being distributed over a larger volume of fluid (Haase and Smith 1989b).

The parameter $\mu = c_0/c_{gr}$ as defined in Haase and Smith (1989b) identifies two broad regimes of supercritical and subcritical in terms of $\mu < 0.7$ or $\mu > 0.7$. The parameter μ is computed similarly for the control run and the four tests, but the equivalent propagating speed of the gravity current in the absence of stratification as defined in Haase and Smith (1989a) must be estimated by a different approach because the heat sink is specified for the current simulations, whereas in the study of Haase and Smith (1989a,b) a cold inflow was injected into the domain. The speed of the gravity current arising from the imposed cooling is, therefore, approximated by the quantity $(Qdl)^{1/3}$ (where Q is the cooling rate of the heat sink; d is the depth of the heat sink; and l is the width of the heat sink) in an unstratified environment and reduced by the opposing ambient flow roughly at the order of the flow speed (Raymond and Rotunno 1989). The propagation speed of the gravity current thus calculated equals 12 m s^{-1} by taking the average speed of the low-level opposing inflow of 4 m s^{-1} as the ambient flow speed. This value for c_{gr} is used to obtain the values listed in Table 5. The simulations for tests H750, H1000, and H1500 (Figs. 15b–d) show bores generated by the gravity current and propagating ahead on the near-surface stable layer. This is consistent with the fact that conditions are subcritical ($\mu > 0.7$), and the gravity current loses its elevated head as the wave disturbance detaches from it. The value of μ for the control run is 0.43, well below the critical value 0.7, indicating that the flow pattern (Fig. 9) is in the supercritical regime (S18, S19, and S20 in Haase and Smith 1989b), which is consistent with the fact that the gravity current keeps its distinct head during the entire integration. For test H500 (Fig. 15a), $\mu = 0.6$, which is close to the critical value, undulations of large-amplitude gravity waves are excited by the head of the gravity current. The comparison indicates that their concept provides a basis for interpreting observations and simulations even with nonuniform ambient wind and stratification as long as the equivalent propagating speed c_{gr} is correctly estimated.

5. Summary and conclusions

This paper presents the first attempt to simulate various gravity wave activities associated with a gravity current using a primitive-equation model to test tentative hypotheses based on detailed Doppler wind profiler and sodar observations. A strong steady-state heat sink is incorporated into the two-dimensional, dry, nonhydrostatic model to generate the observed gravity current, which is physically related to the evaporative cooling of falling precipitation (Seitter 1986). The gravity current produced by the cooling in the model bears remarkable similarity to the observed event, including its propagation speed, the wind shift, the depth of the cold pool, and the temperature drop across its leading edge. Not only are the gross features of the gravity current well simulated, but so are two classes of gravity waves triggered by the gravity current and uniquely documented in the observational study (R93). The simulations produce a train of three 6–8 km wavelength undulations in the lee of the gravity current head, which have the same vertical structure, same vertical extent, and similar vertical velocity amplitudes as the observed waves. The simulations confirm that these are trapped lee-type gravity waves produced by flow over the gravity current head, although the wave energy is trapped primarily by curvature aloft in the wind profile and by an elevated isothermal layer synergetically, rather than by a slightly higher neutral layer as originally hypothesized from the observational analysis. This type of response is analogous to the gravity waves produced by convective-plume-induced undulations in the stable layer capping a convective boundary layer, as studied by Clark et al. (1986). Two-dimensional simulations of convection resulting from a heated boundary layer were presented by Clark et al. (1986). Their results show that in the presence of moderate and strong shear, the eddies in the heated boundary layer represent a form drag to the flow, acting in a similar way to small hills in launching internal gravity waves as the plumes impinge on the stable layer capping the convective boundary layer. The second class of waves, which develop after the lee-type waves, are formed by KH instability on the interface atop the cold pool. The KH waves have wavelengths (2.2–2.7 km) and phase speeds consistent with those inferred in R93 and appear to be at an appropriate altitude.
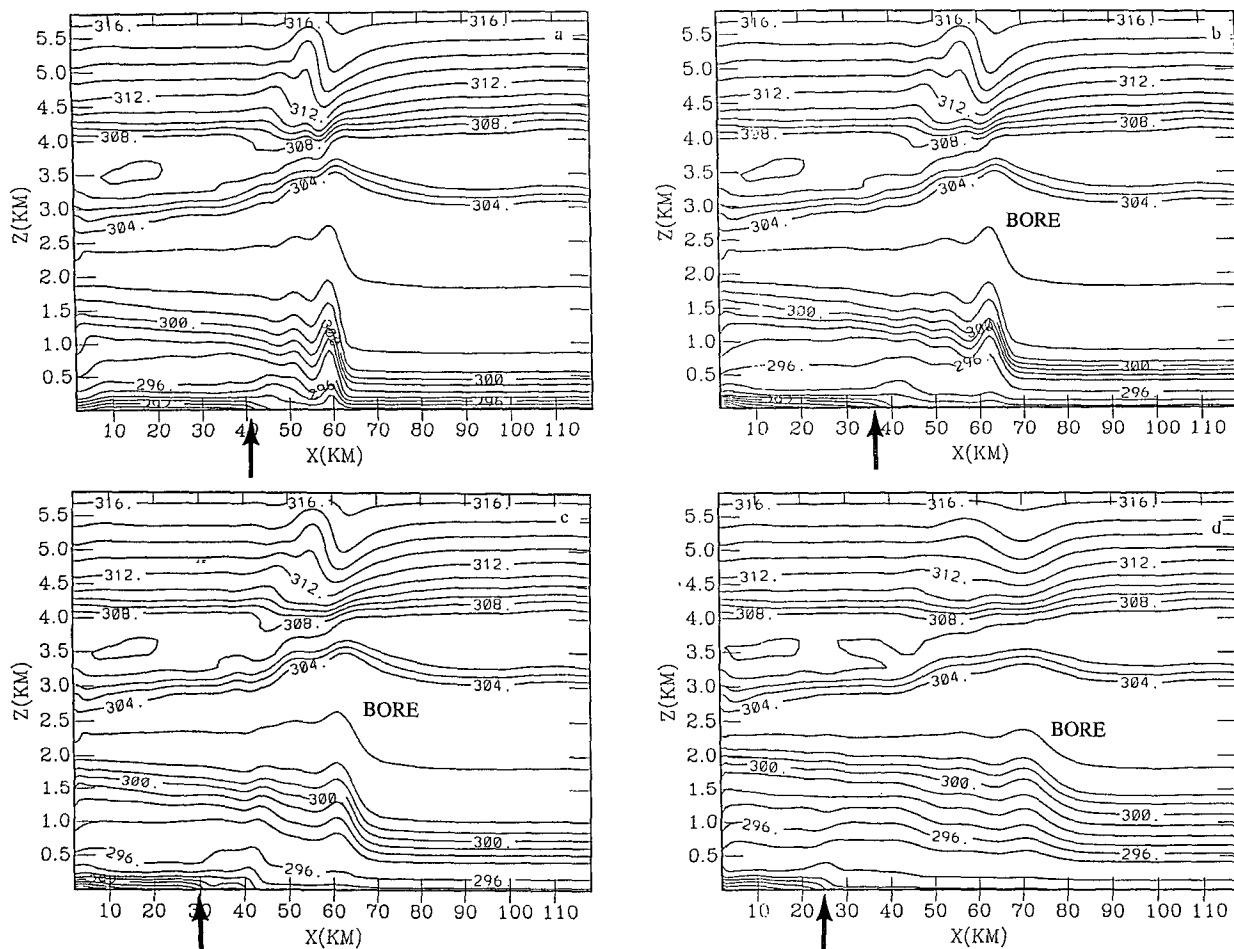
FIG. 15. Isentropes (K) with the coarse resolution at $t = 1.75$ h for the sensitivity tests (a) H500; (b) H750; (c) H1000; (d) H1500. The bores and the leading edge of the gravity current are also indicated in the figure.

In addition to reproducing the observed gravity waves, the simulations agree further with the observations in that no prefrontal bore was produced. Sensitivity tests confirm the earlier interpretation (R93), which was based on the idea that the gravity wave propagation speed in the stable layer must exceed the gravity current propagation speed [i.e., conditions were subcritical (Haase and Smith 1989b)] and that the prefrontal near-surface stable layer was too shallow to allow for the production of such a wave.

Although this study is aided by the simplifications that follow from the event occurring without precipitation at the time of its passage through the observing network described in R93, it has been shown elsewhere that both lee-type waves (Clark et al. 1986) and KH waves (Weckwerth and Wakimoto 1991) can organize clouds, and thus precipitation, under the proper circumstances. Future studies using ground-based and airborne remote-sensing techniques are likely to further our observational documentation of these interesting

mesoscale structures. Combining such observational studies with detailed numerical simulations, such as done here, may result in even greater understanding of the underlying physical processes. It is also hoped that further theoretical studies on dynamic instability will give a more accurate quantitative relationship between the wavelength shortening and the area of small Richardson number (Ri <0.25) in order to predict wave evolution.

REFERENCES

Carbone, R. E., 1982: A severe frontal rainband. Part I: Stormwide hydrostatic structure. *J. Atmos. Sci.*, **39**, 258–279.

Charba, J., 1974: Application of gravity current model to analysis of a squall-line gust front. *Mon. Wea. Rev.*, **102**, 140–156.

Chen, C., 1991: A nested grid, nonhydrostatic, elastic model using a terrain-following coordinate transformation: The radiative-nesting boundary conditions. *Mon. Wea. Rev.*, **119**, 2852–2869.

Clark, T. L., 1977: A small scale numerical model using a terrain following coordinate system. *J. Comput. Phys.*, **24**, 186–215.

——, T. Hauf, and J. P. Kuettner, 1986: Convectively forced internal gravity waves: Results from two-dimensional numerical experiments. *Quart. J. Roy. Meteor. Soc.*, **112**, 889–925.

Crook, N. A., 1988: Trapping of low-level internal gravity waves. *J. Atmos. Sci.*, **45**, 1533–1541.

Doviak, R., and R. Ge, 1984: An atmospheric solitary gust observed with a Doppler radar, a tall tower, and a surface network. *J. Atmos. Sci.*, **41**, 2559–2573.

Droegemeier, K. K., and R. B. Wilhelmson, 1985a: Three-dimensional numerical modeling of convection produced by interacting thunderstorm outflows. Part I: Control simulation and low-level moisture variations. *J. Atmos. Sci.*, **42**, 2381–2403.

——, and ——, 1985b: Three-dimensional numerical modeling of convection produced by interacting thunderstorm outflows. Part II: Variations in vertical wind shear. *J. Atmos. Sci.*, **42**, 2404–2414.

Durran, D. R., 1986: Another look at downslope windstorms. Part I: The development of analogs to supercritical flow in an infinitely deep, continuously stratified fluid. *J. Atmos. Sci.*, **43**, 2527–2543.

Foldvik, A., 1962: Two-dimensional mountain waves—A method for the rapid computation of lee wavelengths and vertical velocities. *Quart. J. Roy. Meteor. Soc.*, **88**, 271–285.

——, and M. G. Wurtele, 1967: The computation of the transient gravity wave. *Geophys. J. Roy. Astron. Soc.*, **13**, 167–185.

Fulton, R., D. S. Zrnic, and R. J. Doviak, 1990: Initiation of a solitary wave family in the demise of a nocturnal thunderstorm density current. *J. Atmos. Sci.*, **47**, 319–337.

Goff, R. C., 1976: Vertical structure of thunderstorm outflows. *Mon. Wea. Rev.*, **104**, 1429–1440.

Gossard, E. E., 1990: Radar research on the atmospheric boundary layer. *Radar in Meteorology*, D. Atlas, Ed., Amer. Meteor. Soc., 477–527.

Haase, S. P., and R. K. Smith, 1989a: The numerical simulation of atmospheric gravity currents. Part I: Neutrally-stable environments. *Geophys. Astrophys. Fluid Dyn.*, **46**, 1–32.

——, and ——, 1989b: The numerical simulation of atmospheric gravity currents. Part II: Environments with stable layers. *Geophys. Astrophys. Fluid Dyn.*, **46**, 35–51.

Holmboe, J., and H. Klieforth, 1957: Investigations of mountain lee waves and airflow over the Sierra Nevada. Final Report, Contract No. AF19(604)-728, University of California, AD No. 133606.

Koch, S. E., P. B. Dorian, R. Ferrare, S. H. Melfi, W. C. Skillman, and D. Whiteman, 1991: Structure of an internal bore and dissipating gravity current as revealed by Raman lidar. *Mon. Wea. Rev.*, **119**, 857–887.

Lin, J. T., and G. J. Binder, 1967: Simulation of mountain lee waves in a wind tunnel. U.S. Army Research Grant DA-AMC-28-043-65-G20, Fluid Dynamics and Diffusion Laboratory, Colorado State University, Fort Collins.

Lin, Y.-L., and R. B. Smith, 1986: Transient dynamics of airflow near a local heat source. *J. Atmos. Sci.*, **43**, 40–49.

——, and H.-Y. Chun, 1991: Effects of diabatic cooling in a shear flow with a critical level. *J. Atmos. Sci.*, **48**, 2476–2491.

Lott, F., and H. Teitelbaum, 1993: Topographic waves generated by a transient wind. *J. Atmos. Sci.*, **50**, 2607–2624.

Mahapatra, P. R., R. J. Doviak, and D. S. Zrnić, 1991: Multisensor observation of an atmospheric undular bore. *Bull. Amer. Meteor. Soc.*, **72**, 1468–1480.

Marks, J. R., 1974: Acoustic radar investigations of boundary layer phenomena. NASA Tech. Rep. CR-2432, Marshall Space Flight Center, Huntsville, AL, 65 pp. [NTIS N7423183.]

Maslowe, S. A., 1973: Finite-amplitude Kelvin-Helmholtz billows. *Bound.-Layer Meteor.*, **5**, 43–52.

Miles, J. W., 1961: On the stability of heterogeneous shear flows. *J. Fluid Mech.*, **10**, 496–508.

Mueller, C. K., and R. E. Carbone, 1987: Dynamics of a thunderstorm outflow. *J. Atmos. Sci.*, **44**, 1879–1898.

Parsons, D. B., M. A. Shapiro, R. M. Hardesty, and R. J. Zamora, 1991: The finescale structure of a west Texas dryline. *Mon. Wea. Rev.*, **119**, 1242–1258.

Queney, P., G. A. Corby, N. Gerbier, H. Koschmeider, and J. Zeirep, 1960: The airflow over mountains. WMO Tech. Note No. 34, 135 pp.

Ralph, F. M., C. Mazaudier, M. Crochet, and S. V. Venkateswaran, 1993: Doppler sodar and radar wind-profiler observations of gravity-wave activity associated with a gravity current. *Mon. Wea. Rev.*, **121**, 444–463.

Raymond, D. J., and R. Rotunno, 1989: Response of a stably stratified flow to cooling. *J. Atmos. Sci.*, **46**, 2830–2837.

Rottman, J. W., and J. E. Simpson, 1989: The formation of internal bores in the atmosphere: A laboratory model. *Quart. J. Roy. Meteor. Soc.*, **115**, 941–963.

Sawyer, J. S., 1960: Numerical calculation of the displacement of a stratified airstream crossing a ridge of small height. *Quart. J. Roy. Meteor. Soc.*, **86**, 326–345.

Scorer, R. S., 1949: Theory of waves in the lee of mountains. *Quart. J. Roy. Meteor. Soc.*, **75**, 41–56.

Seitter, K. L., 1986: A numerical study of atmospheric density current motion including the effects of condensation. *J. Atmos. Sci.*, **43**, 3068–3076.

Shapiro, M. A., T. Hampel, D. Rotzoll, and F. Mosher, 1985: The frontal hydraulic head: A micro-α scale (~1 km) triggering mechanism for mesoconvective weather systems. *Mon. Wea. Rev.*, **113**, 1166–1183.

Simpson, J. E., 1987: *Gravity Currents: In the Environment and the Laboratory.* John Wiley & Sons, 244 pp.

——, and R. E. Britter, 1980: A laboratory model of an atmospheric mesofront. *Quart. J. Roy. Meteor. Soc.*, **106**, 485–500.

Thorpe, A. J., M. J. Miller, and M. W. Moncreiff, 1980: Dynamical model of two-dimensional downdraughts. *Quart. J. Roy. Meteor. Soc.*, **106**, 463–484.

Vergeiner, I., and D. K. Lilly, 1970: The dynamic structure of lee wave flow as obtained from balloon and airplane observations. *Mon. Wea. Rev.*, **98**, 220–232.

Wakimoto, R. M., 1982: The life cycle of thunderstorm gust fronts as viewed with Doppler radar and rawinsonde data. *Mon. Wea. Rev.*, **110**, 1060–1082.

Wang, P.-Y., D. B. Parsons, and P. V. Hobbs, 1983: The mesoscale and microscale structure and organization of clouds and precipitation in midlatitude cyclones. Part VI: Wavelike rainbands associated with a cold-frontal zone. *J. Atmos. Sci.*, **40**, 543–558.

Weckwerth, T. M., and R. M. Wakimoto, 1991: Convection initiation associated with a gust front and Kelvin–Helmholtz instability. Preprints, *25th Conf. on Radar Meteorology*, Paris, France, Amer. Meteor. Soc., 454–457.